Research Square

Preprints are preliminary reports that have not undergone peer review.
They should not be considered conclusive, used to inform clinical practice,
or referenced by the media as validated information.

Wrinkles emerge from matrix complementarity in heterogenous biofilms

Adrien Sarlet
University of Copenhagen
Anja K. Ehrmann
University of Copenhagen
Namiko Mitarai
University of Copenhagen
Liselotte Jauffred
lisja@dtu.dk

Technical University of Denmark

Article

Keywords: Biofilm, Escherichia coli, morphology, multi-species, curli, phosphoethanolamine-cellulose, amyloid

Posted Date: March 16th, 2026

DOI: https://doi.org/10.21203/rs.3.rs-9051999/v1

License: This work is licensed under a Creative Commons Attribution 4.0 International License.
Read Full License

Additional Declarations: No competing interests reported.

Version of Record: A version of this preprint was published at npj Biofilms and Microbiomes on June 19th, 2026. See the published version at https://doi.org/10.1038/s41522-026-01048-x.

Article

Wrinkles emerge from matrix complementarity in heterogenous biofilms

Adrien Sarlet[1], Anja K. Ehrmann[1], Namiko Mitarai[1], and Liselotte Jauffred[1,2,*]

[1]The Niels Bohr Institute, University of Copenhagen, Jagtvej 155 A, DK-2200 Copenhagen N, Denmark
[2]DTU Bioengeenering, Technical University of Denmark, Søltofts Pl. Building 221, 2800 Kgs. Lyngby, Denmark
*lisja@dtu.dk

Keywords: Biofilm, Escherichia coli, morphology, multi-species, curli, phosphoethanolamine-cellulose, amyloid

ABSTRACT Biofilms are dynamic communities of microorganisms encased in a self-produced extracellular matrix. These resilient structures pose challenges across nearly all human activities, from healthcare to industry. The mechanical behaviour of a biofilm is shaped by the heterogenous composition of its matrix, both spatially and chemically. In turn, these mechanics influence the biofilm's architecture at micro- and macroscopic scales, driving its complexity and adaptability. Morphologically, this is reflected in mechanical deformations of the biofilm known as wrinkles. In nature, biofilms often host different species of bacteria, allowing for a great diversity of matrix components. Here, we use a combination of two *Escherichia coli* strains as a model for a multispecies biofilm in which each bacterial strain produces one of two complementary matrix fibres: an amyloid protein (curli) or a polysaccharide (phosphoethanolamine-cellulose). Using fluorescence microscopy, we confirm that the two bacterial strains rapidly segregate into isogenic sectors, decreasing local heterogeneity. Furthermore, we show how wrinkles form, both in the homogenous central region of the biofilm, as well as at the boundary between sectors (i.e. where the two matrix producers co-localize). Finally, we show that increasing strain intermixing via the addition of bacteriophages results in thicker, taller wrinkles, irrespective of whether the two fibres are produced by two different strains or co-produced by the same bacteria.

INTRODUCTION

Biofilms form when microorganisms attach to a surface, divide, and embed themselves in a self-secreted extra-cellular matrix of polymeric substances (e.g. polysaccharides, proteins, lipids, and extracellular DNA). Growth in a biofilm structure collectively provides mechanical stability (1), enables nutrient and signal exchange (2, 3), protects bacteria against phage predation (4, 5), and protects against antibiotics (6, 7). Moreover, chemical treatments can either reinforce or weaken the mechanical stability of a biofilm depending on the matrix composition (8). Biofilms are assumed to account for the majority of prokaryotic biomass on Earth (9). They are involved in numerous diseases (10) and, more generally, negatively impact most sectors of human industries (11).

In *Escherichia coli* in particular, the extra-cellular matrix is mainly composed of curli amyloid fibres and phosphoethanolamine-cellulose (pEtN-cellulose) (12–14). The closely related *Salmonella spp.* is also known to produce both curli and pEtN-cellulose (14). Other Enterobacteriaceae were shown to produce curli and/or cellulose (15) while possessing the genes necessary for their pEtN-modification (16). All in all, the distribution of the genes responsible for the production of these two fibres is much more widespread than the few species in which their production was evidenced (16, 17). From *E. coli* populations producing only one of the two fibres, we know that curli-containing biofilms are stiffer (higher Young's modulus) than those containing only pEtN-cellulose (18). Together, these matrix fibres form a composite material that can withstand a higher compressive load than its individual components (18).

When surface attached communities grow, bacteria divide and push against each other. This leads to a build-up of mechanical tension in the community, which can be relieved by the formation of chiral swirls (19), new cell layers (20), bacterial motility (21), or by self-driven ordering of elongated cells (i.e. active nematics) (22, 23). Tension can also be released by the formation of *wrinkles*, which are generally understood as a mechanical buckling instability (24, 25). In other words, when compressive forces (arising from internal stresses) exceed a critical threshold, the biofilm undergoes out-of-plane deformation, resulting in the formation of wrinkles. Although environmental conditions leading to wrinkle formation differ between species, certain factors seem to be decisive, namely nutrient and oxygen availability (26), as well as agar concentration (proxy for substrate elasticity and friction). Specifically, as the outward expansion of the biofilm is opposed by bacteria-substrate friction, compressive stress is building up and the biofilm releases this stress by wrinkling (25, 27, 28). Therefore, in *E. coli*, increasing the concentration of

agar generally promotes wrinkling (29). Although many parameters are known, a clear understanding of the cues that govern the onset and dynamics of wrinkling remain elusive, especially in multi-species biofilms.

In nature, one species can benefit from the matrix of another (30), e.g. *Vibrio cholerae* can protect *E. coli* against the predator bacterium *Bdellovibrio bacteriovorus* (31) or phage T7 (32). However, there are also examples of bacteria cooperating in matrix-formation. Namely, complementary mutant strains of *E. coli* and *Salmonella typhimurium*, each producing one of the two curli subunits (CsgA and CsgB), can, when in immediate proximity, co-seed curli fibres, whereby one bacterium secretes CsgA monomers that polymerize onto the membrane-associated CsgB of the other (33). Furthermore, a mutant *Bacillus subtilis* and *Pantoea agglomerans* were found to form wrinkled biofilms when well-mixed. In this example, *B. subtilis* provided only the peptidic component TasA, while *P. agglomerans* provided the exopolysaccharide (34). During colony formation, stochastic fluctuations and cell-cell mechanics drive co-cultured strains to segregate into large isogenic sectors while competing for nutrients and space (35). This large-scale patterning depends on relative growth rates (36) and inoculation densities (37) and can be influenced by phage predation (38, 39). But little is known about how this affects subsequent matrix formation and wrinkling.

In this study, we ask how the underlying spatial organization of the bacterial colony controls 3D biofilm architecture. We investigate how local cooperation between curli and pEtN-cellulose producing populations impacts wrinkle formation.Using gene recombination, we prepared a pair of (otherwise similar) *E. coli* strains, each producing one specific matrix fibre. We used this combination of strains as a model for multi-species biofilms, where different strain contribute complementary fibres to the extracellular matrix. Combining laser-scanning confocal microscopy and 3D-image analysis, we mapped the biofilms' macroscopic architecture. We evaluated the role of genetic heterogeneity, and found that wrinkles are not restricted to regions where curli and pEtN-cellulose producing strains are well-mixed. Instead, they can also form on the boundaries between isogenic sectors. Lastly, we added the virulent phage T6 to the system to distort the spatial patterning of the colony and investigate subsequent changes in wrinkling. Based on these results, we propose a mechanical model of wrinkle-formation in heterogenous biofilms.

METHODS

Media

M63+xyl The 5× M63 salt solution was composed of 15 g/l anhydrous KH_2PO_4 (≥98.0%, P9791, Sigma-Aldrich), 35 g/l anhydrous K_2HPO_4 (≥99.0%, 60353, Sigma-Aldrich), 10 g/l $(NH_4)_2SO_4$ (≥99.0%, 09978, Sigma-Aldrich), 2.5 ml 20 mM $FeSO_4$ (≥99.5%, 44970, Sigma-Aldrich), 20 mM Na-Citrate (≥99.5%, 71402, Sigma-Aldrich). The M63 minimal agar was composed of 1× M63 salt, 1 µg/ml thiamine hydrochloride (≥99%, T4625, Sigma-Aldrich), 2 mM $MgSO_4$ (≥99.5%, 63138, Sigma-Aldrich), 2 mg/ml xylose (≥99%, W360600, Sigma-Aldrich) and 15 g/l BD Bacto™ agar (10455513, Fisher Scientific) dissolved in Millipore water.

M9 agar The M9 agar was composed of 2 g/l glucose (22720, Serva), 1× M9 salts, 2 mM $MgSO_4$ (0168, JT Baker), 100 µM $CaCl_2$ (2461, Chemsolute), 1× trace elements and 0.5 µg/ml thiamine hydrochloride (T4625, Sigma-Aldrich) and 15 g/l BD Bacto™ agar (10455513, Fisher Scientific) dissolved in Millipore water. 5× M9 salts consist of 34 g/l Na_2PO_4, 15 g/l KH_2PO_4, 2.5 g/l NaCl (27810.295, VWR) and 5 g/l NH_4Cl (09711, Fluka). 2000× trace elements consist of 37 mM $FeCl_3$, 7 mM $ZnSO_4$, 2.3 mM $CuSO_4$, 5.9 mM $MnCl_2$, 2.5 mM $CoCl_2$, 1.6 mM Na_2EDTA, pH8. 50 µM $NiCl_2$ was added when appropriate for counter-selection against *tetA*.

LB agar The regular LB agar was composed of 10 g/l Gibco™ Bacto™ tryptone (16279751, Fisher Scientific), 5 g/l Gibco™ Bacto™ yeast extract (16279781, Fisher Scientific), 5 g/l NaCl (≥99%, S9888, Sigma-Aldrich) and 15 g/l BD Bacto™ agar (10455513, Fisher Scientific) dissolved in Millipore water. When specified, the LB agar was supplemented with 30 µg/ml

Strain	Name	Genotype	Matrix composition	References
MS613	Cur^+	MG1655 K-12 (F- *λ- ilvG- rfb-50 rph-1*)	curli	(21, 40)
RMV612	∅	MG1655 *csgAB::kan*	/	(19)
AS011	Cur^+pCe^+	MS613 *bcsQ+*	curli, pEtN-cellulose	This work
AS012	pCe^+	AS011 *csgAB::kan*	pEtN-cellulose	This work

Table 1: Strains used in this work.

kanamycin sulphate (≥95%, K1377, Sigma-Aldrich), 50 µg/ml spectinomycin dihydrochloride pentahydrate (≥62%, S-9007, Sigma) or 50 µg/ml tetracycline hydrochloride (T7660, Sigma-Aldrich).

Salt-free agar The salt-free agar was composed of 10 g/l Gibco™ Bacto™ tryptone (16279751, Fisher Scientific), 5 g/l Gibco™ Bacto™ yeast extract (16279781, Fisher Scientific) and 15 g/l BD Bacto™ agar (10455513, Fisher Scientific) dissolved in Millipore water. When specified, the salt-free agar was supplemented with 30 mg/l Direct Red 23 (≥30%, 212490, Sigma-Aldrich) or 40 mg/l Congo Red (≥35%, C6767, Sigma-Aldrich), previously filter-sterilized and added to the melted agar immediately before pouring.

Bacterial strains and culture

Background MS613 (40) is a MG1655 K-12 strain producing curli amyloid fibres but not pEtN-cellulose (Cur$^+$) due to an early stop codon in *bcsQ* in *E. coli* K-12 strains. AR3110 (12) is a W3110 (i.e. K-12) derivative in which *bcsQ* was repaired, thereby restoring pEtN-cellulose production.

AS011 From MS613, a xylose auxotrophic mutant was created by P1 transduction from the *xylA* mutant of the Keio collection (JW3537) (41), *xylA* being distant from *bcsQ* by approximately 35 kbp, followed by selection on kanamycin. The resulting xylose auxotroph was then *repaired* by P1 transduction from AR3110, followed by selection on M63 + xylose medium. The resulting strains were subsequently inoculated on salt-free agar for biofilm growth. One of those strains, AS011, showed similar wrinkling to that of AR3110. Thus, that strain's *bcsQ* was restored simultaneously with *xylA* and therefore, it produces both curli fibres and pEtN-cellulose (Cur$^+$pCe$^+$). The P1 transduction protocol was adapted from (42, 43).

AS012 From AS011, *csgBA* was mutated by P1 transduction from RMV612 (19), which produces neither curli nor pEtN-cellulose (∅), thereby yielding AS012, which produces pEtN-cellulose but not curli (pCe$^+$).

Introduction of fluorescent markers For each of the four strains MS613, RMV612, AS011 and AS012 variants were constructed expressing either *gfp* or *rfp*. The fluorescent reporter genes were integrated into the genome of the strains following the protocols for λ-Red recombineering and *tetA* dual-selection protocol as described by Bayer et al. (44). Briefly, strains were first transformed with pSIM19 (45). The expression of the λ-Red proteins was induced by 20 min incubation at 42 °C. The cells were made electrocompetent by three rounds of washing in ice-cold water. 4 ng/µl gel-purified dsDNA or 400 nM ssDNA oligonucleotide were used for the transformation (final concentration in 50 µl competent cells). In the first step, a J23100-*gfp-tetA* dsDNA cassette, amplified from the genomic DNA of the strain SEGA007 (44) was integrated into the *glmS-pstS* intergenic region of all strains. Successful recombinants were selected on LB agar containing 50 µg/ml tetracycline. Candidate colonies were restreaked at least once on LB + tetracycline and subsequently verified by colony PCR and Sanger sequencing (Eurofinns Genomics, Germany). In order to exchange the *gfp* and *tetA* genes for *rfp*, or to remove *tetA* for a marker-less labelling with *gfp*, a second round of recombineering and *tetA* counter-selection was performed. Cells were transformed with either a *rfp* dsDNA fragment amplified from the genomic DNA of strain SEGA-007-*rfp* (44) or a ssDNA oligonucleotide containing the appropriate homology sequences to remove *tetA* from the J23100-*gfp-tetA* cassette. To select for the correct recombinants, cells were first recovered in LB medium overnight, washed in 1× M9 salts and a dilution row plated on M9 glucose plates supplemented with 50 µM $NiCl_2$. Candidate colonies were restreaked twice on LB agar and verified by colony PCR and Sanger sequencing.

Biofilm culture A liquid culture was inoculated from a single colony and grown overnight in LB medium. The optical density of the resulting bacterial suspension was measured at 600 nm (OD_{600}). The bacteria were diluted to reach a concentration corresponding to OD_{600} = 0.4. Four drops of 2 µl each were typically inoculated onto a salt-free agar Petri dish. The resulting biofilms were sealed with Parafilm ® and grown at 28 °C for 5 days. For biofilms inoculated from a mix of two different bacterial strains, each liquid culture was brought to OD_{600} = 0.4 before mixing them in the indicated proportion. Immediately before imaging, one biofilm was cut out from the agar and placed on a glass slide. The glass slide was flipped because the fluorescence and confocal microscopes were inverted.

Phage infection The biofilms grown in the presence of T6 phages were inoculated as described above. After 6 h of incubation at room temperature, 1 µl of T6 phage suspension ($6 \cdot 10^8$ pfu/ml) was spotted either 1 mm away from the dried bacterial drop (side inoculation), or was added on top of the dried bacterial drop (centre inoculation). The method was derived from (38, 39). The biofilms were then incubated at 21 °C (room temperature) for 10 days before imaging. The phage suspension was diluted in salt free LB broth from a phage stock solution prior to infection.

Note that the phage experiments were performed under different growth conditions than the other experiments, following the protocol by Ruan et al. closely (38). They were also performed in a different lab facility using different stocks to prepare the growth medium.

To test susceptibility of strains to phage T6, liquid cultures of all bacterial strains were inoculated in LB medium from overnight cultures. Cultures were incubated at 37 °C until they reached exponential growth. 100 µl of bacterial culture were then mixed with 3 ml top agar (8 g/l NaCl (27810.295, VWR), 6 g/l BD Bacto™ agar (10455513, Fisher Scientific)) and poured on top of a fresh LB agar plate. After the top agar solidified, 2 µl of concentrated phage stock solution were added as a drop on top of the agar. Plates were incubated at 37 °C.

The possibility of phage T6 infection in salt free LB medium was evaluated by measuring OD_{600} growth curves of RMV612 (∅) in a FLUOstar Omega microtiter plate reader (BMG LABTECH, Ortenberg, Germany). After an overnight preculture in standard LB broth, RMV612 was diluted 1:250 into fresh salt-free LB broth (without agar) and incubated at 37 °C under shaking. When reaching exponential phase ($OD_{600} \approx 0.3 - 0.4$) the bacteria were diluted again 1:10 into a 96-well microtiter plate containing salt-free LB broth and incubated at 37 °C for 45 min. Then, dilutions of a phage stock prepared in salt-free medium were added, the plate sealed with a breathable film and OD_{600} was measured every 5 min over the course of 20 h. The control samples were grown in LB medium supplemented with 10 mM $MgSO_4$. The equivalent amount of salt-free medium was added to the phage-free control samples.

Cross-section Following 5 or 10-day growth, 20 µg/ml chloramphenicol (≥98%, C0378, Sigma-Aldrich) was added to the Petri dish containing the biofilm to be sectioned. Prior to sectioning, the biofilm (and surrounding agar) was cut out and placed in a small Petri dish. There, the biofilm was embedded in agar also supplemented with 20 µg/ml chloramphenicol: ~12.5 ml 50 °C agar was poured into the dish without directly pouring on the biofilm. The role of chloramphenicol is to prevent further colonisation of bacteria into the newly poured agar. Once the top agar had solidified, the biofilm was cross-sectioned with a scalpel, flipped, and transferred into a glass-bottomed dish for imaging. The cross-sectioning procedure was simplified from (29).

Imaging and analyses

Brightfield microscopy Brightfield images with and without Congo red, were acquired using a Reshape Imaging System (Reshape Biotech, Copenhagen, Denmark) using top light illumination without optical magnification.

Fluorescence microscopy We used a Nikon ECLIPSE Ti microscope (Nikon, Tokyo, Japan) equipped with a 4× air immersion objective (Nikon, Plan Fluor, 4×/0.13, ∞/1.2 WD 16.5) and paired with an Andor Neo camera (Andor, Belfast, UK). GFP and RFP were excited by an Hg lamp using the FITC (FITC Filter Cube Set, Olympus, York, UK) and Texas Red cubes (Texas Red™ Filter Cube Set, Nikon, Tokyo, Japan), respectively. The tiles were stitched (20% overlap, pixel size: 1.625 µm) automatically upon acquisition by the microscope's native software: NIS-Elements Advanced Research (4.13.03, Nikon).

Confocal scanning microscopy We used a Leica DMI6000 CS SP5 (Leica, Wetzlar, Germany) with the Ar (488 nm) and HeNe (543 nm) laser lines sequentially to excite GFP and RFP, respectively. We used a 5× air objective (Leica, N Plan, 5×/0.12 PH0) for the images corresponding to the height maps while a 40× (Leica, N Plan, 40×/0.55) air objective was used for cross-sections.

Height maps and profiles Using custom-made Matlab (Matlab R2023, The MathWorks, Inc) procedures and starting from z-stack images with two channels (GFP and RFP), the maximum intensity projection over the (z)-dimension of each channel was computed individually. Both projections were normalised so that their intensities could be compared. Every pixel of the image was assigned one colour (green or red) by comparing the two projections for that pixel. Then for every pixel in (x, y) in the original z-stack, the z-coordinate of the maximum intensity pixel was determined in the colour channel previously assigned to that pixel. Then all z-coordinates were translated to the minimum value of the pixel and converted to metric units. This resulted in an (x, y)-image mapping the height of the brightest pixels: h-map. For wrinkle profiles, the h-map was used to find maximum wrinkle heights in pixel i over the length of the wrinkle: $l_i = l_{i-1} + \sqrt{(x_i - x_{i-1})^2 + (y_i - y_{i-1})^2}$.

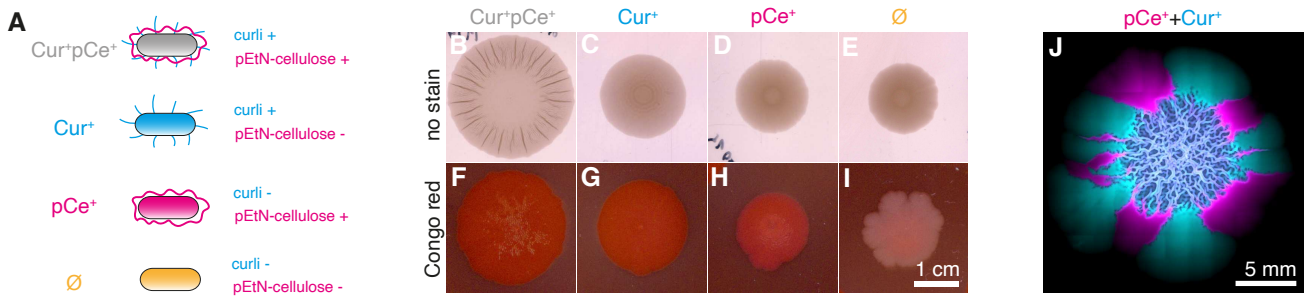


Figure 1: **pEtN-cellulose reconstituted in curli-producing *E. coli***
E. coli biofilms grown for 5 days on salt-free agar (B-E) and on salt-free agar supplemented with Congo red (F-I). **A**: Illustration of the strain set used in this study. **B+F:** AS011 producing both curli and pEtN-cellulose (Cur^+pCe^+); **C+G:** MS613 producing only curli (Cur^+); **D+H:** AS012 producing only pEtN-cellulose (pCe^+) and **E+I:** RMV612 producing neither curli, nor pEtN-cellulose (∅). Scale bar: 1 cm. Note in particular the difference of shade between H and I, which otherwise appear identical in D and E. **J:** Pseudo-coloured fluorescence image of a two-strain biofilm (pCe^++Cur^+) initially mixed in a 1:1 ratio grown for 5 days on salt-free agar. Scale bar: 5 mm.

RESULTS

pEtN-cellulose reconstituted in curli-producing *E. coli*

Starting from a standard curli-producing but cellulose deficient (Cur^+) *E. coli* K-12 strain, MG1655, we repaired the production of pEtN-cellulose by P1 transducing *bcsQ* from AR3110, in which it had been previously repaired (12). The resulting strain produces both curli and pEtN-cellulose (Cur^+pCe^+). From there, we mutated the curli producing genes *csgBA* by P1 transduction from the strain producing none of the two fibres (∅) (19), to create a pEtN-cellulose-only strain (pCe^+) [Figure 1A and Table 1].

Grown on salt-free agar, Cur^+pCe^+ biofilms exhibit long radial wrinkles [Figure 1B] and a larger diameter than biofilms formed by other strains [Supplementary Figure S1]. Cur^+ biofilms form a previously described (12) characteristic ring pattern around the central region [Figure 1C, Supplementary Figure S2] but both the pCe^+ strain and the ∅ mutant, producing none of the fibres, have smooth phenotypes [Figure 1D, E]. We confirmed the production of pEtN-cellulose in the pCe^+ strain by supplementing the salt-free agar with Congo red, which binds both amyloid fibres and cellulose (12, 46) [Figure 1H, I]. Interestingly, the presence of Congo red also influences the biofilm phenotypes: The Cur^+pCe^+ biofilm showed shallower wrinkling [Figure 1F], while the pCe^+ biofilm exhibited dense wrinkles in the central region, otherwise absent without Congo red [Figure 1H]. A weakening of the interaction between curli and pEtN-cellulose could explain the relatively smoother phenotype in the Cur^+pCe^+ strain. Such an effect by Congo red was already reported in *E. coli* UTI89 by Reichhardt *et al.* (46), who also reported increased wrinkling in their pEtN-cellulose-only strain in the presence of Congo red, due to a higher affinity of the dye for pEtN-cellulose than for curli.

We inoculated a suspension of the Cur^+ and pCe^+ strains (each labelled with a unique fluorescent reporter) in equal proportions. Once the colony expanded beyond the well-mixed area of the inoculation droplet, the population segregated into large isogenic sectors, each formed by a strain with the ability to produce one of the matrix fibres [Figure 1J]. As segregation is the result of small variations at the fast-growing colony front, this happens before the onset of matrix production. Specifically, the fibre production starts 48-72 hours after entry into stationary phase. Therefore, we can use this system to test how a given spatial patterning affect the overall biofilm morphology. A zoom-in on the central region shows dense wrinkling and a pattern of curli and pEtN-cellulose producers (cyan and magenta) mixed at subwrinkle scales [Supplementary Figure S3A]. The corresponding height map (*h*-map) emphasises the surface structure of the complex architecture in the mixed biofilms [Supplementary Figure S3B-C]. We verified that curli and pEtN-cellulose fibres were present in both mixed and mono-strain biofilms by imaging biofilm cross-sections stained with Direct Red 23 [Supplementary Figure S4]. Based on this confirmation and to support readability, we will henceforth refer to strains capable of producing these fibres as *producers*. However, while remembering that matrix production varies in different layers of the biofilm and that certain subpopulations might not produce any fibres at all.

Wrinkles are formed on the boundaries of curli and pEtN-cellulose-rich regions

Outside of the homogenous central region, the two strains are only in contact at the boundary between their respective isogenic sectors [Figure 2A]. We verified that there was no strain stratification by cross-sectioning the biofilm [Figure 2B]. Despite this

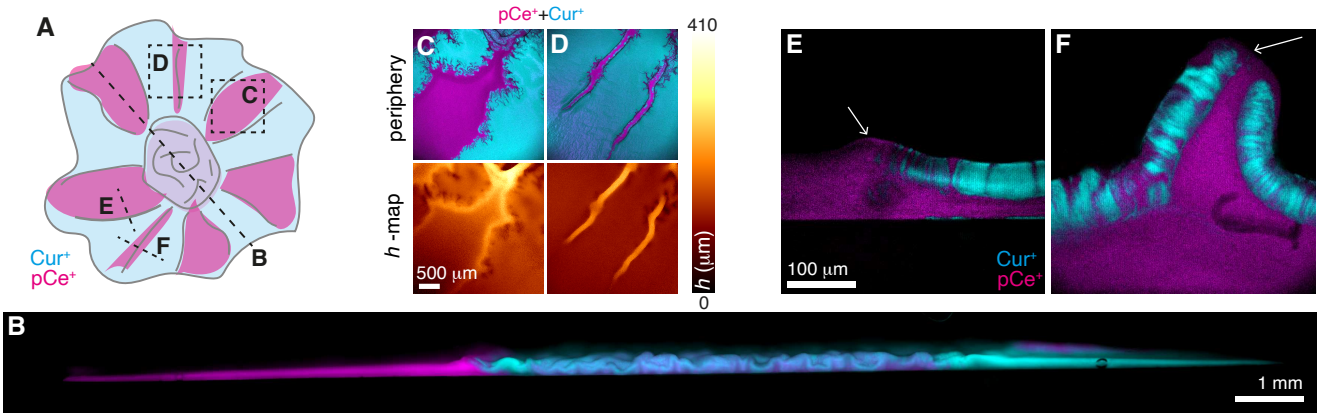


Figure 2: **Wrinkles are formed on the boundaries of curli and pEtN-cellulose-rich regions.**
A: Sketch of a two-strain biofilm from a 1:1 mixed suspension (Cur^++pCe^+). The letters indicate from where in the colonies the images in (C-D, black boxes) and the cross-sections in (B,E-F, black lines) were taken. **B:** Pseudo-coloured wide-field fluorescence microscopy of a cross-section through a biofilm grown from a 1:1 suspension of curli- and pEtN-cellulose-producing strains (Cur^++pCe^+). Scale bar: 1 mm. **C-D:** Pseudo-coloured maximum-intensity projections (periphery) and the respective height map (*h*-map) from the outer region of the two-strain colony (Cur^++pCe^+). Scale bar: 500 µm. **E-F**: Pseudo-coloured confocal imaging of cross-sections of wrinkles in the outer region, at the boundary between two larger sectors (E) and through a thin pEtN-cellulose sector (F). Scale bar: 100 µm

.

strong demixing of genotypes, the biofilm formed radial wrinkles at the sector boundaries exclusively. We did not observe any wrinkles in isogenic sectors, which indicates a synergistic interplay between the strains, each producing one matrix fibre. Morphologically, two types of radial wrinkles were observed. First, wrinkles formed on the boundaries between large adjacent sectors of mono-strains, each producing one of the fibres [Figure 2C]. Alternatively, wrinkles formed around a thin pCe^+ sector enclosed between two Cur^+ sectors [Figure 2D]. We cross-sectioned sector boundaries of mixed pCe^++Cur^+ biofilms (i.e. cross-sections perpendicular to wrinkles) to characterize the two different types of wrinkles [Figure 2E-F]. In both cases, the pCe^+ bacteria (magenta) dominate the ridge (white arrows) of the wrinkles. We also found that at the sector boundary, the mixed pCe^+ and Cur^+ layer was present at the surface, while the pCe^+ bacteria extended underneath [Figure 2E]. In both cases pCe^+ filled up the cavity of the wrinkle [Figure 2E-F]. Staining with Direct Red 23 confirms the presence of both matrix fibres in the wrinkle structure [Supplementary Figure 4D]. The patterning of the two fibres in the wrinkle corresponds to the patterning of the two strains at the interaction interface, confirming the non-diffusive nature of the matrix fibres and the presence of pEtN-cellulose inside the wrinkle cavities.

Wrinkles are formed in curli-sparse regions

As curli and pEtN-cellulose fibres possess distinct mechanical properties (18, 47), they contribute differently to *E. coli* biofilm architecture. Curli is considered to be the stiff – but brittle – component that is able to withstand a large compressive load. In contrast, pEtN-cellulose acts as a glue-like tension-bearing matrix component (48). We therefore investigated whether the wrinkle formation we observed on the boundaries between curli and pEtN-cellulose-rich regions requires both fibres or rather arises from the interruption of curli sectors. To do so, we mixed the Cur^+ with the ∅ strain, which produces neither curli nor pEtN-cellulose. We found stronger wrinkling in the centre region of the pCe^++Cur^+ biofilm than in the ∅+Cur^+ biofilm [Figure 3A-C]. This indicates that ∅-dilution of the Cur^+ strain creates a more viscous material capable of dissipating the stress. Nevertheless, when considering the segregated periphery of the biofilm, the thin sectors (pCe^+ or ∅) squeezed between two Cur^+ sectors rose in wrinkle structures in both cases [Figure 3D-E]. The wrinkles had similar topography and maximal heights ($h \approx 100$ µm), similar in height to the wrinkles of the pCe^++Cur^+ mix' central region [Figure 3A]. These results indicate that wrinkle formation at the heterogenous sector boundaries of a multi-strain biofilm is the consequence of an interruption of rigid (curli-rich) sectors and does not necessarily require the presence of pEtN-cellulose. Therefore, wrinkling here is (at least partially) determined by the elastic properties of the biofilm.

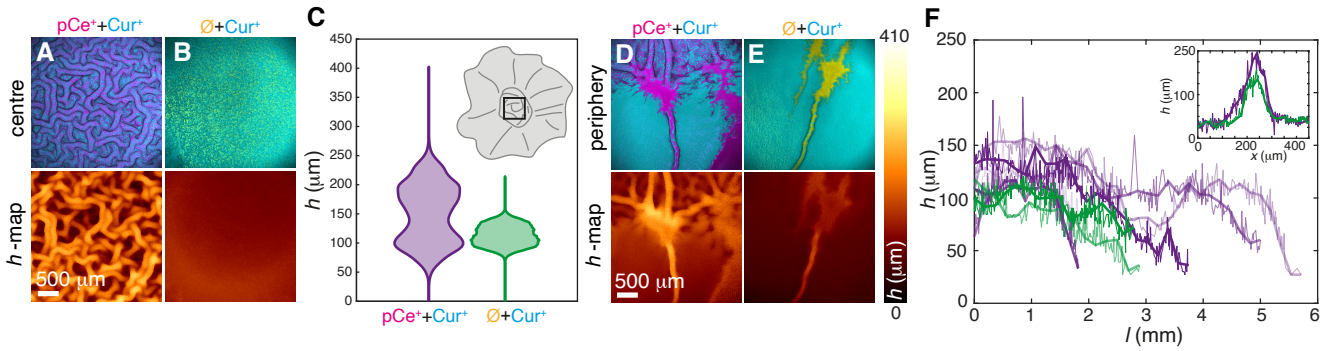


Figure 3: **Wrinkles are formed in curli-sparse regions.**
A-B: Pseudo-coloured maximum-intensity projections (centre) and the corresponding height map (h-map) of a region-of-interest from the central region of two-strain colonies of (pCe^++Cur^+) (A) and the curli-producer and the strain producing neither curli nor pEtN-cellulose (∅+Cur^+) (B), see legends. Scale bar: 500 µm. Colour bar in (E) and note that the data in A is the same as in Supplementary Figure S3. **C:** Height distributions of the h-maps in (A-B). The inset is a sketch of the biofilms, where the central region-of-interest is indicated (black box). $N = 262144$ in both cases. **D-E:** Pseudo-coloured maximum-intensity projections (periphery) and the corresponding height map (h-map) of a region-of-interest from the outer region of the two-strain colonies (pCe^++Cur^+) (D) and (∅+Cur^+) (E), see legends. Scale bar: 500 µm. **F:** Maximum wrinkle heights, h, versus the length of the radial wrinkle, l,measured from the centre and outwards. Examples of wrinkles from two-strain colonies of pCe^++Cur^+ (purple) and ∅+Cur^+ (green), where the thicker full line is a spline-like smoothed curve-fit. Inset: h versus the axis perpendicular to the wrinkle, x, for pCe^++Cur^+ (purple) and ∅+Cur^+ (green). Colour scale corresponds to the main plot.

Phage predation changes biofilm spatial organization through increased intermixing

We have established that biofilm morphology reflects the underlying multi-strain colony and that wrinkles form sub-sequent to growth-driven spatial organization. In the next step, we decided to manipulate this organization through bacteriophage infection. Indeed, Ruan and co-authors have previously demonstrated that predation by phage T6 on a growing colony increases intermixing and slows down spatial segregation through increased cell-cell alignment (38). In other words, we used phage predation to enforce homogeneity into our otherwise heterogenous biofilm matrix. First, we confirmed that all strains were sensitive to phage T6 and that the phage could infect and spread in salt-free medium [Supplementary Figure S5]. Then we added phage T6 to a mixed (pCe^++Cur^+) biofilm shortly after initial inoculation and observed how segregation was suppressed during range expansion [Figure 4A]. As a consequence, wrinkling ceased to be restricted to the central region and predefined sector boundaries. Instead, pCe^++Cur^+ biofilm morphology resembled a Cur^+pCe^+ biofilm under phage T6 predation, characterized by large wrinkles with large separation (i.e. wavelength) [Figure 4B]. Specifically, the wrinkle expansion includes a broadening (in the surface plane) and a h-raise [Figure 4C] for the radial wrinkles, reaching approximately 500 µm in both directions [Figure 4D]. From cross-sections of these radial wrinkles, we confirmed that the composite material (i.e. pCe^+ and Cur^+ under phage T6 predation) retained diversity throughout the biofilm. This also resulted in different patterning of the wrinkles [Figure 4E, cf. Figure 2E-F]. Moreover, one large wrinkle often consisted of a small set of wrinkles [Figure 4E]. Alternatively, we also inoculated the phages a few mm away from the nascent colony. The result was that the phenotypical change (i.e. large wrinkles with large separation) was restricted to the area of contact with the phages [Figure 4F]. The above observations are consistent with phage T6 erasing faster-growing biofilm fronts, which prevents segregation of strains (38). However, it is worth noting that T6 predation did not shape our biofilm fronts to mono-layers of bacteria, in contrast to what was reported for similar *E. coli* strains (38). Instead, biofilms retained their volume [Supplementary Figure S6], indicating some protection (e.g. shielding) from matrix fibres.

DISCUSSION

Biofilm-formation relies on the secretion of an extracellular matrix that constitutes a robust three-dimensional architecture. The resulting surface wrinkles depend on cell-cell interactions, substrate adhesion, and the mechanical properties of the matrix fibres. For example, curli and pEtN-cellulose have either synergistic or antagonistic effects on bacterial adhesion, depending on the substrate (49–51). Multiple studies have shown that the distribution of matrix component is heterogenous, even in isogenic systems (18, 52), and that heterogeneity arises from intricate regulation of matrix production (52). To capture this spatial heterogeneity, agent-based models have incorporated substrate friction, adhesion, and nutrient dynamics (53–55). In

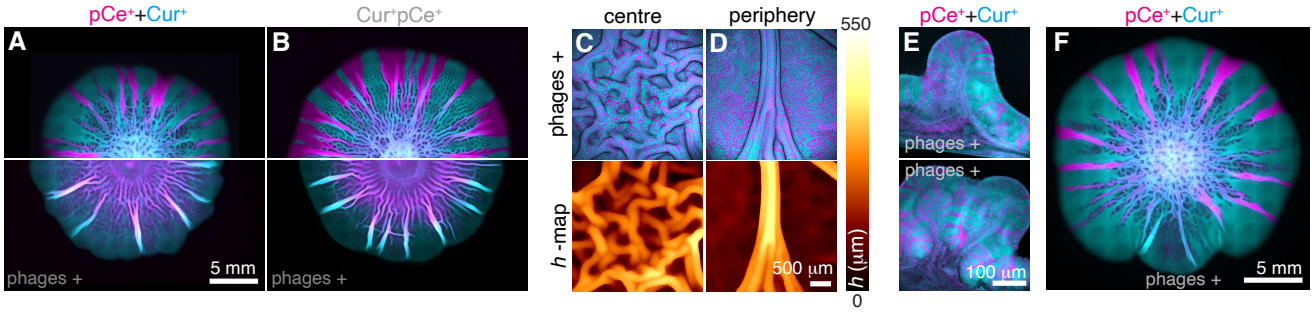


Figure 4: **Phage predation changes biofilm spatial organization through increased intermixing.**
A-B: Pseudo-coloured fluorescence images of pCe$^+$+Cur$^+$ biofilm (A) and Cur$^+$pCe$^+$ biofilm grown of isogenic but coloured (magenta+cyan) strains (B). In both cases, they where grown for 10 days on salt-free agar with (phages+) or without phage T6 added (see legends). Scale bar: 5 mm. The change in phenotype of the negative controls (compared to Figure 1-4) is due to a change in growth conditions (see Methods). **C-D:** Pseudo-coloured maximum-intensity projections and their respective height maps (*h*-map) from the central region (B) and outer periphery (C) region of the two-strain colony (Cur$^+$+pCe$^+$) with T6 phages added (phages+). Scale bar: 500 µm. **E**: Pseudo-coloured confocal imaging of cross-sections of wrinkles in the outer region (periphery) in two-strain colonies (Cur$^+$+pCe$^+$) with T6 phages added (phages+). **F:** Pseudo-coloured fluorescence images of the two-strain biofilm (pCe$^+$+Cur$^+$) initially mixed in a 1:1 ratio grown for 10 days on salt-free agar with phage T6 added next to the biofilm (see legends). Scale bar: 5 mm.

addition, small adhesion variabilities were proposed to locally lower the wrinkling threshold, while nutrient availability shapes the global pattern (56).

Building on this framework, we sought to decipher heterogeneity arising from the spatial organization of multiple strains contributing to a biofilm, rather than from variations in gene expression. To this end, we investigated matrix complementarity by mixing *E. coli* curli- and pEtN-cellulose producers (Cur$^+$+pCe$^+$) with distinct mechanical properties (18, 48). The resulting surface-attached biofilms had a homogeneous composite centre and a heterogenous periphery composed of mono-strain sectors separated by well-defined boundaries.

In the homogeneous central region of the mixed biofilm, we observed intense wrinkling, even exceeding that of the strain producing both fibres (Cur$^+$pCe$^+$). However, wrinkling intensity was sensitive to subtle growth variations (compare Figure 1B and Figure 4A with Supplementary Figure S2). These variations may be reflected in substrate mechanics (57–59), signalling (3), or matrix production (52).

In contrast, in the heterogeneous peripheral region, wrinkles were restricted to boundaries between curli (Cur$^+$) and pEtN-cellulose (pCe$^+$) sectors, where complementary matrix fibres interact. Furthermore, under specific conditions, wrinkles formed on the boundary of sectors of the strain producing neither fibres (∅). These observations favours the conclusion that tension is building up in curli-rich regions of high rigidity and that this tension is released by spontaneous wrinkling in the more flexible (cellulose-rich) regions.

From the cross-sections, we found biofilms detaching from the substrate (i.e. delaminated), similar to what has been reported for *Pseudomonas aeruginosa* (60). This contrasts with the internal delamination of stratified layers described for *Vibrio cholerae* (28). We also found pEtN-cellulose producers filled the wrinkle interior, making it unlikely that these wrinkles could serve as transport channels (12, 14, 61), as in *B. subtilis* (62). However, it remains unresolved whether cellulose-producing cells progressively squeeze between leaflet and substrate or occupy gaps created by curli-layer delamination. In either case, this suggests that there could be more pEtN-cellulose producers in the biofilm, than what appears from the top views [Supplementary Figure S3A].

Biofilms have been shown to protect against phage infection. Mature *E. coli* biofilms resist phage T7 via curli-mediated inhibition of phage transport and binding (5), and in *Staphylococcus epidermidis*, biofilm architecture strongly influences phage efficacy (63). Phages can also degrade extracellular fibres or exploit them as receptors (64–66). However, none of these activities have been observed for phage T6, and we did not test interactions between T6 and curli or pEtN-cellulose fibres as such (67). Instead, phage exposure was used to delay segregation and, thereby, affect wrinkling. Indeed, we found that mono-strain (Cur$^+$pCe$^+$) and mixed (pCe$^+$+Cur$^+$) biofilms had similar morphologies under infection. To our knowledge, this is the first demonstration of phage-induced changes in biofilm wrinkling. Following Ruan *et al.* (38, 39), we attribute this to changes in the directional order in the biofilm. While phage-mediated killing at the colony front increases alignment of rod-shaped bacteria (behind the front), diversity is retained and the merging of sectors is delayed. This indicates that the

resulting composite matrix resembled that of mono-strain biofilms.

Directional elastic instability is a general feature of anisotropic thin films, where wrinkle orientation and spacing depend on the alignment of the material director relative to the compressive stress (68). In biofilms, orientational ordering of rod-shaped bacteria generates anisotropic stress distributions (69), correlating with aspect ratio (22), adhesion (23, 70), and matrix formation (in *V. cholerae* (69, 71)). Thus, phage-induced alignment likely creates mechanical anisotropy and may bias wrinkling toward fewer, more dominant radial modes. Phage infection may additionally alter stress-signalling pathways, controlling matrix production (3).

These observations were integrated within an extended mechanical framework, covering both the homogenous biofilm interior and the heterogenous periphery [Figure 5]. Mechanical *thin sheet* models (72) regard biofilms as flexible material expanding radially, while the adhesion of the film to its substrate generates friction in the direction of the biofilm centre (anti-parallel to expansion). This leads to a build-up of shear stress in the biofilm, relieved by wrinkling. This description covers the homogeneous biofilm interior [Figure 5A]. To predict wrinkling size and periodicity, homogenous biofilms have been described as continuous thin elastic plates and wrinkles as Föppl-von Kármán equations (based on Young's modulus, Gauchy tensors, and Poisson ratio) (73, 74). Furthermore, adding additional thin plates with different elastic properties can account for colony-substrate friction, gradients (e.g. of air, humidity, and nutrients) (27, 28, 75), and viscous relaxation (76). To encompass the peripheral region, we propose to incorporate spatial heterogeneity as thin (curli-rich) plates interrupted by softer tension-bearing (pEtN-cellulose) regions [Figure 5B]. Within this heterogeneous elastic landscape, stress accumulates in stiff domains and is released at compliant interfaces, explaining the emergence of wrinkles at sector boundaries.

Phage-induced alignment further modifies this mechanical landscape by imposing directional elasticity and enhancing compositional homogeneity, thereby, shifting wrinkle periodicity and regularity [Figure 5C-F]. In this way, we provide a unified mechanical interpretation linking matrix complementarity, spatial organization, and phage-mediated re-organization to global biofilm architecture [Figure 5].

Our study establishes *Escherichia coli* as a versatile model for investigating wrinkle formation in Gram-negative biofilms. By reconstituting the two essential matrix components (curli amyloid fibres and phosphoethanolamine-cellulose) we created a fully controllable two-strain system that mimics multi-species heterogeneity. This approach enables systematic explorations of how matrix composition and spatial organization govern mechanical instabilities such as wrinkling and manifest in the macroscopic biofilm morphology. Given the growing clinical threat of Gram-negative biofilms (77), this model system provides a valuable platform to decipher the mechanics of biofilms and develop strategies to mitigate biofilm-associated problems.

Acknowledgments The authors thank Sine Lo Svenningsen and Bertil Kent Gummesson for access to the Keio collection and to their microbiology facilities, Cécile Bidan and Jeannette Steffen for providing the AR3110 strain, and Stanley Brown for his mentoring regarding the P1 transduction.

Funding Statement This research was supported by grants from the Independent Research Fund Denmark grant no. DFF 0165-00032B and grant no. DFF 0165-00103B (LJ), Danish National Research Foundation grant no. DNRF137, and Novo Nordisk Foundation NERD grant no. NNF21OC0068775 (NM) and Synergy grant no. NNF23OC0086712 (LJ).

Competing Interests None.

Data Availability Statement The experimental data supporting the plots provided in this study are uploaded to the NBI research collection: https://sid.erda.dk/sharelink/m4fU81ZXS0. DOI will follow.

Author Contributions AS conceived the original idea. AS and AKE performed the experiments: both contributed to the strain engineering and to the imaging. AS did the data analysis. LJ and NM supervised the project. All authors discussed the results and contributed to the final manuscript.

REFERENCES

1. Gloag, E. S., S. Fabbri, D. J. Wozniak, and P. Stoodley, 2020. Biofilm mechanics: Implications in infection and survival. Biofilm 2:100017. https://linkinghub.elsevier.com/retrieve/pii/S2590207519300176.

2. Bavaharan, A., and C. Skilbeck, 2022. Electrical signalling in prokaryotes and its convergence with quorum sensing in Bacillus. BioEssays 44. https://onlinelibrary.wiley.com/doi/10.1002/bies.202100193.

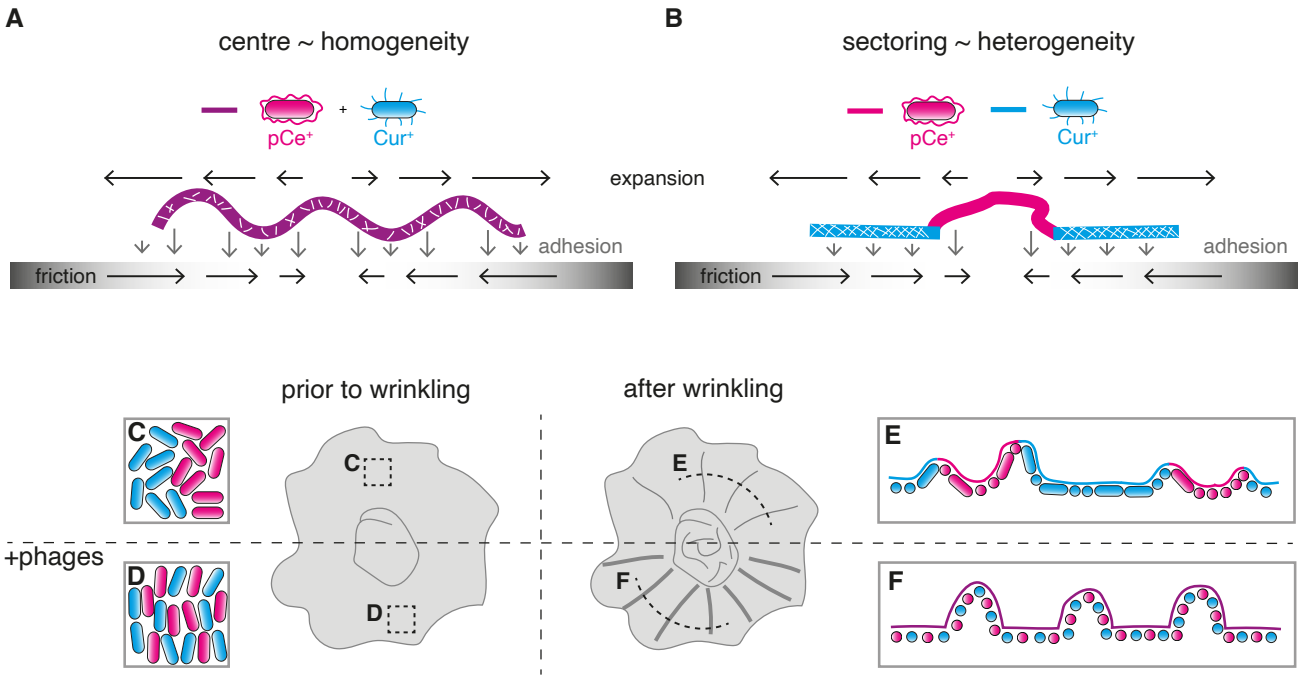


Figure 5: **Wrinkling in homogenous and heterogenous biofilms.**
A-B: Illustration of wrinkle-formation in the homogenous central region (A) and on the heterogenous sector boundaries (B). The expansion of the biofilm is counteracted by the friction at the biofilm-agar interface (black arrows) and adhesion (gray arrows). The composite material of both strains and fibres (purple) is semi-rigid (dilute network of white lines) and the mono strain sectors of pEtN-cellulose (pCe^+) and curli (Cur^+) producers are soft or rigid (tight network of white lines), respectively.
C-F: Conceptual model of orientational order prior to wrinkling (C-D) or after wrinkling (E-F) with phages (C+E) or without (D+F). The letters indicate from where in the colonies the top views (C-D, black boxes) and the cross-sections (E-F, black lines) were taken. Note that while the illustrations of the orientational order prior to wrinkling builds on earlier reports (38), the orientational order after wrinkling is an interpretation of the results of this study.

3. Hengge, R., 2020. Linking bacterial growth, survival, and multicellularity – small signaling molecules as triggers and drivers. Current Opinion in Microbiology 55:57–66. https://linkinghub.elsevier.com/retrieve/pii/S1369527420300308.

4. Bond, M. C., L. Vidakovic, P. K. Singh, K. Drescher, and C. D. Nadell, 2021. Matrix-trapped viruses can prevent invasion of bacterial biofilms by colonizing cells. eLife 10:1–15. https://elifesciences.org/articles/65355.

5. Vidakovic, L., P. K. Singh, R. Hartmann, C. D. Nadell, and K. Drescher, 2017. Dynamic biofilm architecture confers individual and collective mechanisms of viral protection. Nature Microbiology 3:26–31. https://www.nature.com/articles/s41564-017-0050-1.

6. Liu, H. Y., E. L. Prentice, and M. A. Webber, 2024. Mechanisms of antimicrobial resistance in biofilms. npj Antimicrobials and Resistance 2:27. https://www.nature.com/articles/s44259-024-00046-3.

7. Bjarnsholt, T., 2013. The role of bacterial biofilms in chronic infections. APMIS 121:1–58. https://onlinelibrary.wiley.com/doi/10.1111/apm.12099.

8. Tallawi, M., M. Opitz, and O. Lieleg, 2017. Modulation of the mechanical properties of bacterial biofilms in response to environmental challenges. Biomaterials Science 5:887–900. https://pubs.rsc.org/en/content/articlelanding/2017/bm/c6bm00832a.

9. Flemming, H.-C., and S. Wuertz, 2019. Bacteria and archaea on Earth and their abundance in biofilms. Nature Reviews Microbiology 17:247–260. http://www.nature.com/articles/s41579-019-0158-9.

10. Perry, E. K., and M.-W. Tan, 2023. Bacterial biofilms in the human body: prevalence and impacts on health and disease. Frontiers in Cellular and Infection Microbiology 13:1–24. https://www.frontiersin.org/articles/10.3389/fcimb.2023.1237164/full.

11. Cámara, M., W. Green, C. E. MacPhee, P. D. Rakowska, R. Raval, M. C. Richardson, J. Slater-Jefferies, K. Steventon, and J. S. Webb, 2022. Economic significance of biofilms: a multidisciplinary and cross-sectoral challenge. npj Biofilms and Microbiomes 8:42. https://www.nature.com/articles/s41522-022-00306-y.

12. Serra, D. O., A. M. Richter, and R. Hengge, 2013. Cellulose as an Architectural Element in Spatially Structured Escherichia coli Biofilms. Journal of Bacteriology 195:5540–5554. https://journals.asm.org/doi/10.1128/JB.00946-13.

13. Serra, D. O., and R. Hengge, 2021. Bacterial Multicellularity: The Biology of Escherichia coli Building Large-Scale Biofilm Communities. Annual Review of Microbiology 75:269–290. https://www.annualreviews.org/doi/10.1146/annurev-micro-031921-055801.

14. Thongsomboon, W., D. O. Serra, A. Possling, C. Hadjineophytou, R. Hengge, and L. Cegelski, 2018. Phosphoethanolamine cellulose: A naturally produced chemically modified cellulose. Science 359:334–338. https://www.sciencemag.org/lookup/doi/10.1126/science.aao4096.

15. Zogaj, X., W. Bokranz, M. Nimtz, and U. Römling, 2003. Production of Cellulose and Curli Fimbriae by Members of the Family Enterobacteriaceae Isolated from the Human Gastrointestinal Tract. Infection and Immunity 71:4151–4158. https://journals.asm.org/doi/10.1128/IAI.71.7.4151-4158.2003.

16. Römling, U., and M. Y. Galperin, 2015. Bacterial cellulose biosynthesis: diversity of operons, subunits, products, and functions. Trends in Microbiology 23:545–557. https://linkinghub.elsevier.com/retrieve/pii/S0966842X15001201.

17. Dueholm, M. S., M. Albertsen, D. Otzen, and P. H. Nielsen, 2012. Curli Functional Amyloid Systems Are Phylogenetically Widespread and Display Large Diversity in Operon and Protein Structure. PLoS ONE 7:e51274. https://dx.plos.org/10.1371/journal.pone.0051274.

18. Siri, M., A. Sarlet, R. Ziege, L. Zorzetto, C. Sotelo Guzman, S. Amini, R. Hengge, K. G. Blank, and C. M. Bidan, 2025. Mechanical Comparison of Escherichia coli Biofilms with Altered Matrix Composition: A Study Combining Shear-Rheology and Microindentation. ACS Biomaterials Science & Engineering 11:4523–4536. https://pubs.acs.org/doi/10.1021/acsbiomaterials.5c00261.

19. Jauffred, L., R. Munk Vejborg, K. S. Korolev, S. Brown, and L. B. Oddershede, 2017. Chirality in microbial biofilms is mediated by close interactions between the cell surface and the substratum. The ISME Journal 11:1688–1701. https://www.nature.com/articles/ismej201719.

20. Copenhagen, K., R. Alert, N. S. Wingreen, and J. W. Shaevitz, 2021. Topological defects promote layer formation in Myxococcus xanthus colonies. Nature Physics 17:211–215. https://www.nature.com/articles/s41567-020-01056-4.

21. Cordero, M., N. Mitarai, and L. Jauffred, 2023. Motility mediates satellite formation in confined biofilms. The ISME Journal 17:1819–1827. https://www.nature.com/articles/s41396-023-01494-x.

22. van den Berg, N., K. Thijssen, T. T. Nguyen, M. Cordero, A. García Vázquez, N. Mitarai, A. Doostmohammadi, and L. Jauffred, 2025. Emergent collective alignment gives competitive advantage to longer cells during range expansion. Nature Communications .

23. Nijjer, J., C. Li, M. Kothari, T. Henzel, Q. Zhang, J.-S. B. Tai, S. Zhou, T. Cohen, S. Zhang, and J. Yan, 2023. Biofilms as self-shaping growing nematics. Nature Physics 19:1936–1944. https://www.nature.com/articles/s41567-023-02221-1.

24. Asally, M., M. Kittisopikul, P. Rué, Y. Du, Z. Hu, T. Çağatay, A. B. Robinson, H. Lu, J. Garcia-Ojalvo, and G. M. Süel, 2012. Localized cell death focuses mechanical forces during 3D patterning in a biofilm. Proceedings of the National Academy of Sciences 109:18891–18896. https://pnas.org/doi/full/10.1073/pnas.1212429109.

25. Krishnan, N., J. Knight, C. Tropini, L. Ruiz Pestana, and D. Fusco, 2025. The what, when, where, and why of wrinkly morphology in biofilms. Biophysics Reviews 6. https://pubs.aip.org/bpr/article/6/3/031301/3354863/The-what-when-where-and-why-of-wrinkly-morphology.

26. Kolodkin-Gal, I., A. K. Elsholz, C. Muth, P. R. Girguis, R. Kolter, and R. Losick, 2013. Respiration control of multicellularity in Bacillus subtilis by a complex of the cytochrome chain with a membrane-embedded histidine kinase. Genes & Development 27:887–899. http://genesdev.cshlp.org/lookup/doi/10.1101/gad.215244.113.

27. Fei, C., S. Mao, J. Yan, R. Alert, H. A. Stone, B. L. Bassler, N. S. Wingreen, and A. Košmrlj, 2020. Nonuniform growth and surface friction determine bacterial biofilm morphology on soft substrates. Proceedings of the National Academy of Sciences 117:7622–7632. https://pnas.org/doi/full/10.1073/pnas.1919607117.

28. Yan, J., C. Fei, S. Mao, A. Moreau, N. S. Wingreen, A. Košmrlj, H. A. Stone, and B. L. Bassler, 2019. Mechanical instability and interfacial energy drive biofilm morphogenesis. eLife 8. https://elifesciences.org/articles/43920.

29. Ziege, R., A.-M. Tsirigoni, B. Large, D. O. Serra, K. G. Blank, R. Hengge, P. Fratzl, and C. M. Bidan, 2021. Adaptation of Escherichia coli Biofilm Growth, Morphology, and Mechanical Properties to Substrate Water Content. ACS Biomaterials Science & Engineering 7:5315–5325. https://pubs.acs.org/doi/10.1021/acsbiomaterials.1c00927.

30. Yang, L., Y. Liu, H. Wu, N. Høiby, S. Molin, and Z. Song, 2011. Current understanding of multi-species biofilms. International Journal of Oral Science 3:74–81. https://www.nature.com/ijos/journal/v3/n2/abs/ijos201112a.html.

31. Wucher, B. R., J. B. Winans, M. Elsayed, D. E. Kadouri, and C. D. Nadell, 2023. Breakdown of clonal cooperative architecture in multispecies biofilms and the spatial ecology of predation. Proceedings of the National Academy of Sciences 120:2017. https://pnas.org/doi/10.1073/pnas.2212650120.

32. Winans, J. B., B. R. Wucher, and C. D. Nadell, 2022. Multispecies biofilm architecture determines bacterial exposure to phages. PLOS Biology 20:e3001913. http://dx.doi.org/10.1371/journal.pbio.3001913.

33. Zhou, Y., D. Smith, B. J. Leong, K. Brännström, F. Almqvist, and M. R. Chapman, 2012. Promiscuous Cross-seeding between Bacterial Amyloids Promotes Interspecies Biofilms. Journal of Biological Chemistry 287:35092–35103. https://linkinghub.elsevier.com/retrieve/pii/S0021925820626588.

34. Yannarell, S. M., G. M. Grandchamp, S.-y. Chen, K. E. Daniels, and E. A. Shank, 2019. A Dual-Species Biofilm with Emergent Mechanical and Protective Properties. Journal of Bacteriology 201. https://journals.asm.org/doi/10.1128/JB.00670-18.

35. Eigentler, L., F. A. Davidson, and N. R. Stanley-Wall, 2022. Mechanisms driving spatial distribution of residents in colony biofilms: an interdisciplinary perspective. Open Biology 12. https://royalsocietypublishing.org/doi/10.1098/rsob.220194.

36. Hallatschek, O., and D. R. Nelson, 2010. Life at the front of an expanding population. Evolution 64:193–206. https://academic.oup.com/evolut/article/64/1/193/6854125.

37. van Gestel, J., F. J. Weissing, O. P. Kuipers, and A. T. Kovács, 2014. Density of founder cells affects spatial pattern formation and cooperation in Bacillus subtilis biofilms. The ISME Journal 8:2069–2079. http://www.nature.com/articles/ismej201452.

38. Ruan, C., J. Ramoneda, A. Kan, T. J. Rudge, G. Wang, and D. R. Johnson, 2024. Phage predation accelerates the spread of plasmid-encoded antibiotic resistance. Nature Communications 15:5397. https://www.nature.com/articles/s41467-024-49840-7.

39. Ruan, C., D. P. Vinod, and D. R. Johnson, 2025. Phage-mediated peripheral kill-the-winner facilitates the maintenance of costly antibiotic resistance. Nature Communications 16:5839. https://www.nature.com/articles/s41467-025-61055-y.

40. Bachmann, B. J., 1996. Derivations and genotypes of some mutant derivatives of Escherichia coli K-12. In F. C. Neidhardt, editor, Escherichia coli and Salmonella: cellular and molecular biology, ASM Press, Washington D.C., volume 2, 2460–2488.

41. Baba, T., T. Ara, M. Hasegawa, Y. Takai, Y. Okumura, M. Baba, K. A. Datsenko, M. Tomita, B. L. Wanner, and H. Mori, 2006. Construction of Escherichia coli K-12 in-frame, single-gene knockout mutants: the Keio collection. Molecular Systems Biology 2. https://www.embopress.org/doi/10.1038/msb4100050.

42. Miller, J. H., 1972. Experiments in molecular genetics. Cold Spring Harbor Laboratory, New York. https://archive.org/details/experimentsinmol0000mill/page/n3/mode/2up.

43. Thomas J. Silhavy, L. W. E., Michael L. Berman, 1984. Experiments with Gene Fusions. Cold Spring Harbor Laboratory, N. Y.

44. Bayer, C. N., M. Rennig, A. K. Ehrmann, and M. H. H. Nørholm, 2021. A standardized genome architecture for bacterial synthetic biology (SEGA). Nature Communications 12:5876. https://www.nature.com/articles/s41467-021-26155-5.

45. Datta, S., N. Costantino, and D. L. Court, 2006. A set of recombineering plasmids for gram-negative bacteria. Gene 379:109–115. https://linkinghub.elsevier.com/retrieve/pii/S0378111906002927.

46. Reichhardt, C., O. A. McCrate, X. Zhou, J. Lee, W. Thongsomboon, and L. Cegelski, 2016. Influence of the amyloid dye Congo red on curli, cellulose, and the extracellular matrix in E. coli during growth and matrix purification. Analytical and Bioanalytical Chemistry 408:7709–7717. http://link.springer.com/10.1007/s00216-016-9868-2.

47. Tyrikos-Ergas, T., S. Gim, J.-Y. Huang, S. Pinzón Martín, D. Varón Silva, P. H. Seeberger, and M. Delbianco, 2022. Synthetic phosphoethanolamine-modified oligosaccharides reveal the importance of glycan length and substitution in biofilm-inspired assemblies. Nature Communications 13:3954. https://www.nature.com/articles/s41467-022-31633-5.

48. Jeffries, J., G. G. Fuller, and L. Cegelski, 2019. Unraveling Escherichia coli 's Cloak: Identification of Phosphoethanolamine Cellulose, Its Functions, and Applications. Microbiology Insights 12:117863611986523. http://journals.sagepub.com/doi/10.1177/1178636119865234.

49. Jeffries, J., W. Thongsomboon, J. A. Visser, K. Enriquez, D. Yager, and L. Cegelski, 2021. Variation in the ratio of curli and phosphoethanolamine cellulose associated with biofilm architecture and properties. Biopolymers 112:1–11. https://onlinelibrary.wiley.com/doi/10.1002/bip.23395.

50. Hollenbeck, E. C., A. Antonoplis, C. Chai, W. Thongsomboon, G. G. Fuller, and L. Cegelski, 2018. Phosphoethanolamine cellulose enhances curli-mediated adhesion of uropathogenic Escherichia coli to bladder epithelial cells. Proceedings of the National Academy of Sciences 115:10106–10111. https://pnas.org/doi/full/10.1073/pnas.1801564115.

51. Saldaña, Z., J. Xicohtencatl-Cortes, F. Avelino, A. D. Phillips, J. B. Kaper, J. L. Puente, and J. A. Girón, 2009. Synergistic role of curli and cellulose in cell adherence and biofilm formation of attaching and effacing Escherichia coli and identification of Fis as a negative regulator of curli. Environmental Microbiology 11:992–1006. https://sfamjournals.onlinelibrary.wiley.com/doi/10.1111/j.1462-2920.2008.01824.x.

52. Serra, D. O., and R. Hengge, 2019. A c-di-GMP-Based Switch Controls Local Heterogeneity of Extracellular Matrix Synthesis which Is Crucial for Integrity and Morphogenesis of Escherichia coli Macrocolony Biofilms. Journal of Molecular Biology 431:4775–4793. https://linkinghub.elsevier.com/retrieve/pii/S0022283619301779.

53. Li, B., D. Taniguchi, J. P. Gedara, V. Gogulancea, R. Gonzalez-Cabaleiro, J. Chen, A. S. McGough, I. D. Ofiteru, T. P. Curtis, and P. Zuliani, 2019. NUFEB: A massively parallel simulator for individual-based modelling of microbial communities. PLOS Computational Biology 15:e1007125. https://dx.plos.org/10.1371/journal.pcbi.1007125.

54. Aguilar, B., A. Ghaffarizadeh, C. D. Johnson, G. J. Podgorski, I. Shmulevich, and N. S. Flann, 2018. Cell death as a trigger for morphogenesis. PLOS ONE 13:e0191089. https://dx.plos.org/10.1371/journal.pone.0191089.

55. Jayathilake, P. G., P. Gupta, B. Li, C. Madsen, O. Oyebamiji, R. González-Cabaleiro, S. Rushton, B. Bridgens, D. Swailes, B. Allen, A. S. McGough, P. Zuliani, I. D. Ofiteru, D. Wilkinson, J. Chen, and T. Curtis, 2017. A mechanistic Individual-based Model of microbial communities. PLOS ONE 12:e0181965. https://dx.plos.org/10.1371/journal.pone.0181965.

56. Verma, A. K., A. Mookherjee, C. Tropini, D. Fusco, and L. Ruiz Pestana, 2025. The interplay of adhesion, friction, and nutrient availability in modulating biofilm wrinkling behavior. npj Soft Matter 1:8. https://www.nature.com/articles/s44431-025-00007-4.

57. Nayar, V., J. Weiland, C. Nelson, and A. Hodge, 2012. Elastic and viscoelastic characterization of agar. Journal of the Mechanical Behavior of Biomedical Materials 7:60–68. https://linkinghub.elsevier.com/retrieve/pii/S1751616111001354.

58. Lucia Stecchini, M., M. Del Torre, S. Donda, E. Maltini, and S. Pacor, 2001. Influence of agar content on the growth parameters of Bacillus cereus. International Journal of Food Microbiology 64:81–88. https://linkinghub.elsevier.com/retrieve/pii/S0168160500004360.

59. Ryzhkov, N. V., A. A. Nikitina, P. Fratzl, C. M. Bidan, and E. V. Skorb, 2021. Polyelectrolyte Substrate Coating for Controlling Biofilm Growth at Solid–Air Interface. Advanced Materials Interfaces 8:2001807. https://onlinelibrary.wiley.com/doi/10.1002/admi.202001807.

60. Geisel, S., E. Secchi, and J. Vermant, 2022. The role of surface adhesion on the macroscopic wrinkling of biofilms. eLife 11. https://elifesciences.org/articles/76027.

61. Rooney, L. M., W. B. Amos, P. A. Hoskisson, and G. McConnell, 2020. Intra-colony channels in E. coli function as a nutrient uptake system. The ISME Journal 1–13. http://www.nature.com/articles/s41396-020-0700-9.

62. Wilking, J. N., V. Zaburdaev, M. De Volder, R. Losick, M. P. Brenner, and D. A. Weitz, 2013. Liquid transport facilitated by channels in Bacillus subtilis biofilms. Proceedings of the National Academy of Sciences 110:848–852. https://pnas.org/doi/full/10.1073/pnas.1216376110.

63. Melo, L. D. R., G. Pinto, F. Oliveira, D. Vilas-Boas, C. Almeida, S. Sillankorva, N. Cerca, and J. Azeredo, 2020. The Protective Effect of Staphylococcus epidermidis Biofilm Matrix against Phage Predation. Viruses 12:1076. https://www.mdpi.com/1999-4915/12/10/1076.

64. Nobrega, F. L., M. Vlot, P. A. de Jonge, L. L. Dreesens, H. J. E. Beaumont, R. Lavigne, B. E. Dutilh, and S. J. J. Brouns, 2018. Targeting mechanisms of tailed bacteriophages. Nature Reviews Microbiology 16:760–773. https://www.nature.com/articles/s41579-018-0070-8.

65. Samson, J. E., A. H. Magadán, M. Sabri, and S. Moineau, 2013. Revenge of the phages: defeating bacterial defences. Nature Reviews Microbiology 11:675–687. https://www.nature.com/articles/nrmicro3096.

66. Hu, Q., L. Huang, Y. Yang, Y. Xiang, and J. Liu, 2024. Essential phage component induces resistance of bacterial community. Science Advances 10. https://www.science.org/doi/10.1126/sciadv.adp5057.

67. Visnapuu, A., M. Van der Gucht, J. Wagemans, and R. Lavigne, 2022. Deconstructing the PhageâĂŞBacterial Biofilm Interaction as a Basis to Establish New Antibiofilm Strategies. Viruses 14:1057. https://www.mdpi.com/1999-4915/14/5/1057.

68. Soni, H., R. A. Pelcovits, and T. R. Powers, 2016. Wrinkling of a thin film on a nematic liquid-crystal elastomer. Physical Review E 94:012701. https://link.aps.org/doi/10.1103/PhysRevE.94.012701.

69. Nijjer, J., C. Li, Q. Zhang, H. Lu, S. Zhang, and J. Yan, 2021. Mechanical forces drive a reorientation cascade leading to biofilm self-patterning. Nature Communications 12:6632. https://www.nature.com/articles/s41467-021-26869-6.

70. Zhao, K., B. S. Tseng, B. Beckerman, F. Jin, M. L. Gibiansky, J. J. Harrison, E. Luijten, M. R. Parsek, and G. C. L. Wong, 2013. Psl trails guide exploration and microcolony formation in Pseudomonas aeruginosa biofilms. Nature 497:388–391. https://www.nature.com/articles/nature12155.

71. Yan, J., A. G. Sharo, H. A. Stone, N. S. Wingreen, and B. L. Bassler, 2016. Vibrio cholerae biofilm growth program and architecture revealed by single-cell live imaging. Proceedings of the National Academy of Sciences 113. https://pnas.org/doi/full/10.1073/pnas.1611494113.

72. Genzer, J., and J. Groenewold, 2006. Soft matter with hard skin: From skin wrinkles to templating and material characterization. Soft Matter 2:310.

73. Trejo, M., C. Douarche, V. Bailleux, C. Poulard, S. Mariot, C. Regeard, and E. Raspaud, 2013. Elasticity and wrinkled morphology of Bacillus subtilis pellicles. Proceedings of the National Academy of Sciences 110:2011–2016. https://pnas.org/doi/full/10.1073/pnas.1217178110.

74. Dervaux, J., P. Ciarletta, and M. Ben Amar, 2009. Morphogenesis of thin hyperelastic plates: A constitutive theory of biological growth in the Föppl–von Kármán limit. Journal of the Mechanics and Physics of Solids 57:458–471. https://linkinghub.elsevier.com/retrieve/pii/S0022509608002093.

538 75. Zhang, C., B. Li, X. Huang, Y. Ni, and X.-Q. Feng, 2016. Morphomechanics of bacterial biofilms undergoing anisotropic
539 differential growth. Applied Physics Letters 109. https://pubs.aip.org/apl/article/109/14/143701/32511/
540 Morphomechanics-of-bacterial-biofilms-undergoing.

541 76. Matoz-Fernandez, D. A., F. A. Davidson, N. R. Stanley-Wall, and R. Sknepnek, 2020. Wrinkle patterns in active viscoelastic
542 thin sheets. Physical Review Research 2:013165. https://link.aps.org/doi/10.1103/PhysRevResearch.2.
543 013165.

544 77. World Health Organization, 2024. WHO Bacterial Priority Pathogens List, 2024: bacterial pathogens of public health
545 importance to guide research, development and strategies to prevent and control antimicrobial resistance. Technical report,
546 World Health Organization, Geneva.

Supplementary Files

This is a list of supplementary files associated with this preprint. Click to download.

- SI.pdf